Native point defects in mono and bilayer phosphorene

Sudipta Kundu, Mit H. Naik,* and Manish Jain†
Centre for Condensed Matter Theory, Department of Physics, Indian Institute of Science, Bangalore 560012, India

(Received 13 January 2020; revised manuscript received 2 April 2020; accepted 29 April 2020; published 29 May 2020)

We study the stability and electronic properties of intrinsic point defects, vacancy and self-interstitial, in mono and bilayer phosphorene. We calculate the formation energies, quasiparticle defect states, and charge transition levels (CTLs) of these defects using *ab initio* density functional theory (DFT) and *GW* approximation to the electron self-energy. Using the DFT+*GW* two paths formalism for studying interstitial in monolayer phosphorene, we show that with the inclusion of electrostatic corrections CTLs can be calculated reliably. Our calculations show that all the native point defects have low formation energies 0.9–1.6 eV in neutral state. Furthermore, we find that vacancy in phosphorene behaves as an acceptorlike defect which can explain the *p*-type conductivity in phosphorene. On the other hand, interstitial can show both acceptor- and donorlike behavior.

DOI: 10.1103/PhysRevMaterials.4.054004

I. INTRODUCTION

The discovery of graphene [1,2] has evoked tremendous research in two-dimensional (2D) layered materials. Apart from introducing new physics, 2D materials show promising applications in optophotonic, nanophotonic, sensor devices, etc. [3,4]. However, the semimetallic nature of graphene limits its wide application in electronic devices despite its very high carrier mobility [5]. Transition metal dichalcogenides [6–8] are another important member of this 2D materials family. Unlike graphene, they have a finite band gap, but their low mobility [9] constrains their applications. A few years ago, another 2D material, phosphorene, was exfoliated [10–13] from bulk black phosphorus. Phosphorene, the single or few layer form of black phosphorus, has been drawing much attention since then. In a layer of phosphorene, a phosphorus atom is bonded to three other phosphorus atoms via sp^3 hybridization. This gives rise to a puckered honeycomb structure [14]. The uniqueness of phosphorene is its structural anisotropy which manifests in anisotropic optical, thermal, and transport properties [15–17]. Phosphorene has a direct band gap at the center of the Brillouin zone which ranges from ∼0.3 eV (bulk) to ∼2.1 eV (monolayer) [18]. This change in the band gap with the number of layers is due to quantum confinement and nonlinearity of exchange-correlation functional [19]. Phosphorene based field-effect transistors have shown a hole mobility of 1000 cm^2/Vs and a high on/off current ratio up to 10^5 [10]. The tunability of band gap and mobility depending on the number of layers make the material suitable for electronic, optoelectronic, photoelectric, and FET device applications [20,21].

Presence of defect affects the material properties in different ways. Depending on the charge state of the defect, it can induce free carriers or trap charge and act as a scatterer in the system. Electronic, optical, and magnetic properties can also be altered due to the presence of defects. Hence, an extensive study of defects and their possible charge states is required for defect engineering and proper understanding of material properties. The puckered structure of phosphorene facilitates the formation of various defects [22]. Defects in phosphorene have low formation energy [23] in comparison to defects in graphene [24]. There is experimental evidence of vacancies [25] in phosphorene. While defects can escalate the degradation process of devices [26,27] such as vacancy can increase the oxidization of phosphorene, they can also enhance device performance by introducing desired properties; for example, emission of photons at new frequencies at room temperature [28]. Vacancy and self-interstitial are two low energy native point defects in phosphorene. In general, DFT works well for calculating ground state properties like structures of defects. However, the estimation of the correct charge transition level (CTL) requires the calculation of the energy associated with the change in the electron number at the defect site. This is an excited state property and is not expected to be estimated correctly with Kohn-Sham DFT. While Heyd-Scuseria-Ernzerhof (HSE) functional [29] is an improvement over the generalized gradient approximation [30] and works well for bulk materials, it fails to capture the anisotropic screening in two-dimensional materials properly [31,32]. The combined formalism of many body perturbation theory within *GW* approximation [33,34] and DFT has emerged as a reliable method for calculation of CTL [35,36]. Furthermore, previous DFT calculations have either been performed with a small supercell size [37] or have not taken into account the full anisotropic (not only out-of-plane but also in-plane) dielectric constant of phosphorene while correcting for spurious electrostatic interaction [38–40].

We study structural and electronic properties of vacancy and self-interstitial in mono and bilayer phosphorene. We

*Present address: Department of Physics, University of California at Berkeley, California 94720, USA and Materials Sciences Division, Lawrence Berkeley National Laboratory, Berkeley, California 94720, USA.
†mjain@iisc.ac.in

calculate the formation energies and CTLs of these defects using the DFT+*GW* formalism. Since we employ periodic boundary conditions in our calculations, the charged defect calculations suffer from spurious electrostatic interactions with their periodic neighbors. This problem is more prominent in a 2D material due to reduced screening along the out-of-plane direction. We correct for this spurious interaction systematically by properly modeling the anisotropic dielectric medium. Further, we validate our calculation of CTLs by evaluating CTL of interstitial in monolayer phosphorene following two different paths. With the electrostatic correction to defect levels, the two paths agree within ±100 meV. We find that defects in phosphorene have low formation energies, in the range 0.9–1.6 eV, which is consistent with previous calculations [22]. Our study also shows that vacancy can induce *p* doping supporting the experimental finding of intrinsic *p*-type behavior of phosphorene [10,11,21]. In contrast, interstitial in mono and bilayer can act as both *p*-type acceptor and *n*-type donor. Furthermore, we find that the unoccupied defect levels of neutral defect calculated with DFT and *GW* line up with respect to the vacuum level while the occupied defect levels shift downward in *GW* compared to DFT calculated levels. This paper is organized as follows. Section II describes our methods of calculation which include the details about DFT, *GW*, and the corrections for charged defect calculations. Calculation and results of defects in mono and bilayer phosphorene are presented in Secs. III and IV, respectively.

II. COMPUTATIONAL DETAILS AND METHODOLOGY

All the DFT calculations in this study are performed using the QUANTUM ESPRESSO package [41]. We use a norm-conserving pseudopotential [42] and the exchange-correlation potential is approximated by the generalized gradient approximation proposed by Perdew, Burke, and Ernzerhof (GGA-PBE) [30]. The van der Waals interaction between layers is described by "Grimme-D2" method [43]. The wave functions are expanded in a plane wave basis, with plane waves up to an energy of 60 Rydberg included in the basis. For unit cell calculations we adopt a 14×10×1 Monkhorst-Pack [44] *k*-point sampling of the Brillouin zone. A vacuum space of 15.9 Å is added to the unit cell in the out-of-plane direction to simulate an isolated mono or bilayer. The in-plane lattice constants are found to be 3.30 Å and 4.62 Å for monolayer and 3.31 Å and 4.51 Å for bilayer unit cell, respectively. For the calculation of defects, we construct a 7×5×1 supercell to accommodate the vacancy or the interstitial atom. This size of supercell is chosen to simulate an isolated defect and minimize the interaction between periodic images of defects. The Brillouin zone is sampled with a 2×2×1 *k*-point grid for supercell calculations. All atomic coordinates in supercell containing defect are relaxed using Broyden-Fletcher-Goldfarb-Shanno (BFGS) quasi-Newton algorithm until total energy and forces are converged to 10^{-3} eV and 0.025 eV/Å respectively.

The *GW* [33,34] calculations are performed using the BerkeleyGW package [45]. The number of unoccupied bands are 100 and 125 for unit cell in monolayer and bilayer, respectively. This choice ensures the convergence of the band gap to be better than 0.1 eV. The dielectric matrix is expanded in plane wave with energy up to 12 Ry and extended to finite frequencies using generalized plasmon pole (GPP) [34] model. The Coulomb interaction along the out-of-plane direction is truncated to compute the dielectric matrix and self-energy [46]. The static remainder technique is used to accelerate the convergence of the calculation with the number of empty bands [47]. The Brillouin zone sampling used for *GW* calculations of the unit cell is 21×15×1 (see Supplemental Material [48] for more details on convergence parameters for *GW* calculation). We find the quasiparticle band gap for monolayer to be 2.07 eV which is in good agreement with previous theoretical [49–51] and experimental (scanning tunneling spectroscopy [18] and photoluminescence excitation spectroscopy [52]) studies. The band gap for bilayer is 1.29 eV which is also consistent with previous calculations [50,51]. For the defect calculations with 7×5 supercell in monolayer and bilayer, 3500 and 4300 unoccupied states are used, respectively. We diagonalize the Hamiltonian using PRIMME software [53,54] to generate the large number of unoccupied bands needed in the calculation. The Brillouin zone is sampled using a 3×3×1 *k*-point grid.

The formation energy of an isolated defect is defined as:

$$E_q^f[\vec{\mathrm{R}}_q](E_\mathrm{F}) = E_q[\vec{\mathrm{R}}_q] - E_\mathrm{pristine} + N_\mathrm{P}\mu_\mathrm{P} + q(E_\mathrm{F} + \epsilon_\mathrm{VBM}) + E_\mathrm{corr}(q) \quad (1)$$

where E_pristine is the total energy per supercell of pristine mono or bilayer phosphorene, $E_q[\vec{\mathrm{R}}_q]$ is the total energy of a supercell containing defect in charge state q at its relaxed coordinates $\vec{\mathrm{R}}_q$, N_P is the number of phosphorus atoms added to (or removed from) the supercell to create the defect, μ_P is the chemical potential of a phosphorus atom which is calculated from bulk black phosphorus, ϵ_VBM is the energy of the valence band maximum (VBM) of the pristine cell, E_F is the Fermi level with respect to ϵ_VBM, and $E_\mathrm{corr}(q)$ is the electrostatic correction term.

As discussed previously, simulations of charged defects suffer from an erroneous electrostatic interaction between the defect cell and its images arising due to periodic boundary conditions. As a consequence, formation energies and eigenvalues of defect levels in charged defects are estimated incorrectly. The correction term $E_\mathrm{corr}(q)$ in Eq. (1) removes the spurious electrostatic interactions and includes the potential alignment in formation energy. $E_\mathrm{corr}(q)$ is calculated using the Freysoldt-Neugebauer-Van de Walle (FNV) scheme [55] as implemented in COFFEE code [56]. To calculate the correction term, mono and bilayer phosphorene are modeled as a dielectric slab of width 5.22 Å and 10.44 Å, respectively. The dielectric constants of the slab [57] are calculated using density functional perturbation theory of the QUANTUM ESPRESSO package [41]. The dielectric constants for monolayer phosphorene are 12.5, 18.9, and 1.9 along the zigzag, armchair, and out-of-plane directions respectively. These quantities for bilayer are 13.5, 27.4, and 1.9, respectively. The difference in the in-plane dielectric constants is due to the structural anisotropy of phosphorene. The variation of dielectric constant along the out-of-plane direction with the number of layers is slow [37,58]. The dielectric constant in the out-of-plane direction turns out to be same up to the first place in decimal for both mono and bilayer phosphorene (see Supplemental Material for more details [48]). The charge is

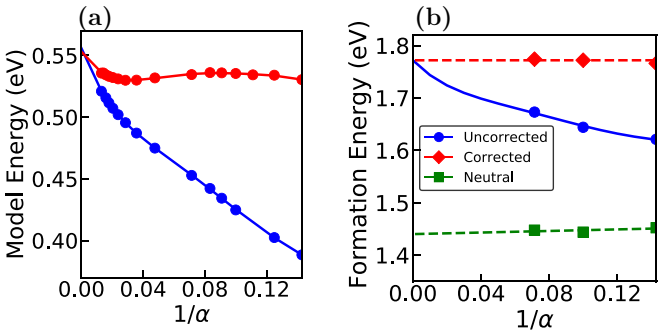

FIG. 1. (a) shows the variation of electrostatic energy of bilayer phosphorene with different supercell sizes. α is the scaling factor. Blue and red curves represent the variation with scaling $\alpha\times\alpha\times\alpha$ and $\alpha\times\alpha\times1.5\alpha$, respectively. In (b) the formation energies of negatively charged interstitial in bilayer phosphorene without and with correction for three different cell sizes are shown by blue circles and red diamonds and extrapolated to infinite limit. The formation energy of neutral interstitial are shown by green squares.

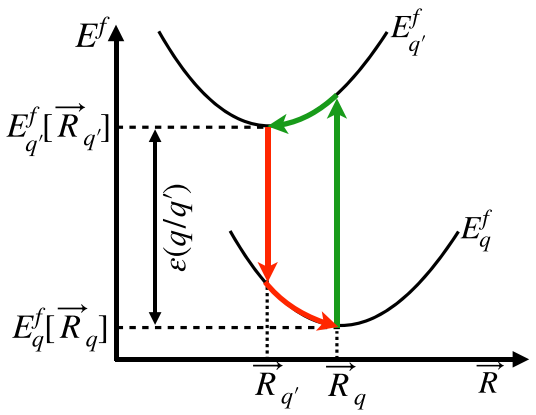

FIG. 2. The figure shows calculation of CTLs following different paths. The straight green and red arrows represent the quasiparticle energies calculated at the equilibrium structures of the defect with charge state q and q', respectively. The curved arrows account for relaxation energies.

modeled as Gaussian distribution whose parameters are taken from DFT calculations. Using this model, the electrostatic energy is calculated for different cell sizes with a uniform scaling parameter α and extrapolated to infinite limit using fifth order polynomial to obtain the value for an isolated defect [57]. The difference between the isolated value and the value for a particular cell size gives the required correction in formation energy for the corresponding cell. To verify our model, we calculate the electrostatic energies of negatively charged interstitial defect in bilayer phosphorene with a model charge for several supercell sizes. Our starting cell is the 7×5 supercell ($\alpha = 7$) for which the in-plane lattice parameters are almost equal. We uniformly scale the cell size along all the three directions and calculate the electrostatic energy [blue curve in Fig. 1(a)]. Further, we perform a different set of scaling calculations starting from a supercell such that the vacuum scaling is different. The scaling factor in these cells along the out-of-plane direction is 1.5 times of those in the in-plane directions [red curve in Fig. 1(a)]. We observe that the electrostatic correction does not change monotonically with the inverse of supercell length which necessitates the several calculations of large supercell to reach the infinite length limit. As a result, a simple 1/L extrapolation from a small supercell size can lead to incorrect isolated value [59,60]. Figure 1(b) shows the formation energies of negatively charged interstitial in bilayer phosphorene without and with correction for supercell sizes 7×5, 10×8, and 14×10. The corrections have been obtained following the blue curve of Fig. 1(a). It can be clearly seen that the corrected formation energies are the same for all the supercells. For comparison we have further included the formation energies of neutral defect in bilayer phosphorene for the same supercell sizes as mentioned above. The formation energies of neutral defect also have no supercell size dependence. This correction is required at the DFT level because the periodic Hartree potential within DFT has spurious long-range Coulomb interaction between the charged cell and its images. We truncate the Coulomb interaction along the out-of-plane direction in *GW* calculation [46,61]. As a result, the Coulomb interaction goes as $\frac{1}{\vec{q}}$ instead of $\frac{1}{\vec{q}^2}$ for small $\vec{q}$. This behavior is consistent with the behavior of Coulomb interaction in 2D. Furthermore, the screened Coulomb interaction also behaves consistently. Due to the truncation, no additional correction is required for *GW* calculations.

The defect CTL $\varepsilon(q/q')$ is defined as the Fermi-level position for which the formation energies of charge states q and q' are equal:

$$\varepsilon(q/q') = \frac{E^f_q[\vec{\mathrm{R}}_q](E_\mathrm{F}=0) - E^f_{q'}[\vec{\mathrm{R}}_{q'}](E_\mathrm{F}=0)}{q'-q}. \quad (2)$$

The CTL can be computed from formation energies within DFT. However, due to band gap underestimation within DFT and the fact that CTL involves change in electron number, significant error arises in the computed CTL. Within the combined DFT and *GW* approach, the CTL [35] is written as:

$$\varepsilon(q/q') = \frac{\left(E^f_q[\vec{\mathrm{R}}_q] - E^f_{q'}[\vec{\mathrm{R}}_q]\right) + \left(E^f_{q'}[\vec{\mathrm{R}}_q] - E^f_{q'}[\vec{\mathrm{R}}_{q'}]\right)}{q'-q} \quad (3)$$

by adding and subtracting term $E^f_{q'}[\vec{\mathrm{R}}_q]$ in the numerator. If the charge states q and q' differ by ±1, the term $(E^f_q[\vec{\mathrm{R}}_q] - E^f_{q'}[\vec{\mathrm{R}}_q])$ can be identified as the quasiparticle energy (E_QP) which is calculated using *GW*. This term accounts for an electron removal or addition to the system. The other term $(E^f_{q'}[\vec{\mathrm{R}}_q] - E^f_{q'}[\vec{\mathrm{R}}_{q'}])$ captures the relaxation energy (E_relax) of the structure due to the change in electron number and is calculated using DFT. Depending on the addition or removal of the electron [Eq. (3)], CTL can be calculated following different paths (Fig. 2). The parabolas in Fig. 2 represent the formation energies as a function of the generalized coordinates of the atoms in the cell. Along one path, we start with the defect in charge state q at its equilibrium coordinates, $\vec{\mathrm{R}}_q$. The E_QP is represented by the green vertical arrow, and E_relax by the green curved arrow. The CTL can also be computed starting with the defect in charge state q', as shown by the red arrows. Since CTL is a thermodynamic quantity, the CTL

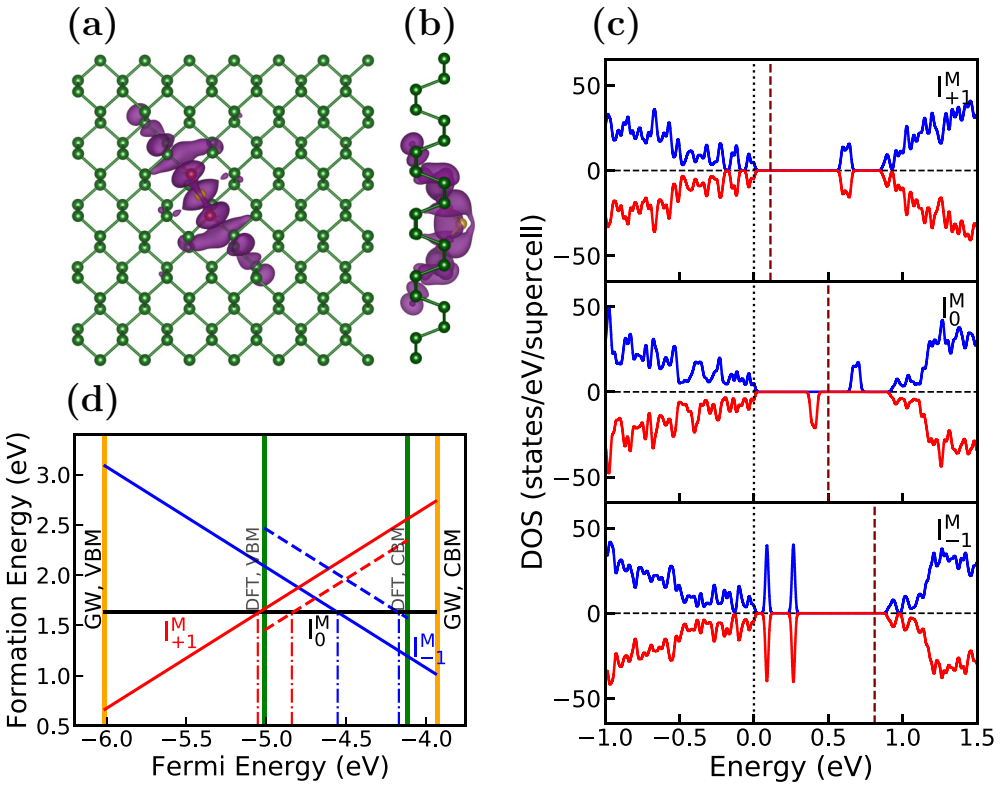

FIG. 3. (a) Top view and (b) side view of interstitial defect in monolayer phosphorene with defect wave function. The isosurface is plotted at the charge density value of 3.4×10^{-3} e/Å^3. The interstitial atom is shown in yellow color and the neighbor atoms are in red. (c) Spin polarized DOS of the interstitial in three charged states. VBM is set to zero and is shown in a black dotted line. Fermi level is marked in a maroon dashed line. Red and blue are for two spin states. (d) CTLs calculated within DFT and DFT+*GW* formalism. The dashed and solid lines represent the formation energies calculated with DFT and DFT+*GW*, respectively, and red, black, and blue are used for +1, 0, and −1 charge states, respectively. Formation energy of neutral defect remains the same. The VBM and CBM are also marked in the figure. We have set the vacuum to zero in the plot.

computed using the two paths should be the same. Note that if the *GW* calculation is performed on charged defects the DFT defect eigenvalues have to be corrected. We calculate the CTLs for interstitial in monolayer phosphorene following two paths [35,62–64] starting from neutral defect ($q = 0$) and charged defect supercells ($q' = +1$ or -1). With the corrected quasiparticle values, the CTLs from different paths agree to within ±100 meV. The details of the calculations are given in the subsequent section.

III. DEFECTS IN MONOLAYER PHOSPHORENE

A. Interstitial

The most stable structure of interstitial in monolayer phosphorene is when the interstitial atom forms two symmetric bonds with two phosphorus atoms in one of the sublayers and resides above the layer [Figs. 3(a) and 3(b)]. Formation of two bonds leaves the interstitial atom with a lone electron which can induce defect states. Spin-polarized calculations reveal two defect states in the band gap. The defect states are localized along one diagonal of the supercell centering the interstitial atom as is shown in the plot of the wave function [Figs. 3(a) and 3(b)]. One of the defect states is occupied in neutral state making the interstitial be stable in all three charge states (+1,0,−1). Figure 3(c) shows the density of states (DOS) for all the charge states. Due to the dispersion along the diagonal direction, the defect bands are broad. Upon accepting an electron, the interstitial atom breaks the symmetry and the bonds become asymmetric. There is no significant relaxation when the defect is positively charged. In the negatively charged interstitial, the defect state appears flatter. This is due to the fact that the defect wave function is more localized. While the defect states are spin split in the neutral state, they become degenerate in both positively and negatively charged states as the electrons get paired in these states. The interstitial defect has low formation energy of 1.63 eV in neutral state. To obtain the formation energy in charged states, we evaluate the correction term ($E_{\rm corr}$) using COFFEE as detailed in Sec. II. The correction using model charge calculation is 0.295 eV. Taking the potential alignment into account, $E_{\rm corr}$ is calculated to be 0.30 eV and 0.26 eV for positively and negatively charged states, respectively. The variation of formation energies of interstitial in charged states, as the Fermi energy is tuned, is shown in Fig. 3(d). Within DFT (red and blue dashed line), the defect changes its state from positive to neutral [$\varepsilon(+1/0)$] at 0.18 eV and from neutral to negative [$\varepsilon(0/-1)$] at 0.84 eV above VBM [Fig. 3(d)]. As already mentioned, to get a better estimate of CTL we perform *GW* calculation on the neutral vacancy to obtain the quasiparticle energy and calculate formation energies within

TABLE I. CTLs of the interstitial along two different paths are reported. *GW* calculation on neutral defect is denoted by path 1 and path 2 represents calculations starting from charged defects. All the energies are reported in eV. E_{QP} is quasiparticle energy and E_{Relax} is the energy associated with relaxing the defect. The correction for the eigenvalue is given by ϵ_{corr}.

	Path 1				Path 2					
	E_{QP}	E_{relax}	ϵ_{corr}	CTL	E_{QP}	E_{relax}	ϵ_{corr}	CTL	Avg. CTL	Difference
$+1/0$	0.71	0.25	0.00	0.96	1.78	−0.19	−0.59	1.00	0.98	0.04
$0/-1$	1.75	−0.27	0.00	1.48	0.46	0.31	0.59	1.36	1.42	0.12

the combined formalism of DFT and *GW*. The solid red and blue line in Fig. 3(d) show the variation of formation energies of positively and negatively charged interstitial, respectively, within DFT+*GW*. The formation energy of neutral defect is the same in DFT and DFT+*GW*. The DFT+*GW* CTLs $\varepsilon(+1/0)$ and $\varepsilon(0/-1)$ are at 0.96 eV and 1.48 eV above VBM, respectively. In this DFT+*GW* calculation, the E_{QP}'s are calculated from the *GW* calculation of the ionization potential and electron affinity of neutral interstitial. CTLs can also be calculated starting from charged defects [Eq. (3)] [35] as described before. The CTLs from two paths and their constituent energies are reported in Table I. To obtain $\varepsilon(+1/0)$, we calculate the electron affinity of positively charged interstitial within *GW*. In this case, the *GW* defect level also has to be corrected [35]. The correction for the defect levels is 0.59 eV [56]. Following this path, $\varepsilon(+1/0)$ is calculated to be 1.00 eV. Similarly, starting from negatively charged interstitial and calculating ionization energy we obtain $\varepsilon(0/-1)$ to be 1.36 eV. The differences between the CTLs obtained from the neutral and charged cell calculations lie within the error of *GW* calculation (0.1 eV). As a result, the CTLs due to interstitial in monolayer phosphorene are deep in the gap. The presence of both $\varepsilon(+1/0)$ and $\varepsilon(0/-1)$ CTLs implies that interstitial in monolayer phosphorene can show both donor- and acceptor-type behaviors.

B. Vacancy

Upon removing one phosphorus atom from phosphorene, there are two possible monovacancy structures: MV-(55|66) [Figs. 4(a) and 4(b)] and MV-(5|9) [Figs. 4(c) and 4(d)] [22]. MV-(55|66) has a symmetric structure. In this structure, the atom closest to the vacancy is connected with 4 P atoms instead of the usual coordination of 3. In contrast, the closest atom to the vacancy in MV-(5|9) moves and the system rearranges such that it bonds with three atoms. The formation energy of MV-(5|9) is lower than that of MV-(55|66) by 330 meV per defect. In order to estimate the barrier between the two structures, we perform a climbing image nudged elastic band (CI-NEB) calculation as implemented in PASTA package [65]. Figure 4(e) shows how the formation energy changes as MV-(55|66) transforms to the more stable MV-(5|9) structure. The energy barrier between the two structures is found to be only 5 meV. Due to this low barrier, we expect the defect to always be in the MV-(5|9) structure. Hence, for all further calculations, we only consider the more stable structure, MV-(5|9).

We investigate the MV-(5|9) vacancy in three charge states: neutral, positive, and negative. We perform spin-polarized calculations. The neutral vacancy gives rise to an unoccupied flat band in the band gap. The DOS calculation [Fig. 4(f)] shows a state 0.23 eV above the VBM. We plot the corresponding wave function in Figs. 4(c) and 4(d). It is clear that the wave function of this site is localized around the vacancy along a diagonal of the supercell. We can understand the origin of this state as follows: a P atom neighboring the vacancy forms two bonds and has a dangling bond which gives rise to the flat band in the gap. The filled defect state lies deep within the valence band and we found that the vacancy is not stable in a positive charge state. The defect can accommodate an electron and change its state to negatively charged state. Upon accepting an electron, the system rearranges itself such that both the defect bands are in the band gap and they become degenerate [Fig. 4(f)]. It is to be noted that MV-(55|66) also induces defect states but those are within the valence band. These states hybridize with the valence band states making the defect always negatively charged. However, this configuration is always higher in energy than negatively charged MV-(5|9).

We calculate the formation energies of MV-(5|9) in neutral and negatively charged states. In Fig. 4(g) the black line represents the formation energy of neutral vacancy. The vacancy has a formation energy of 1.42 eV in the neutral state. Due to this low formation energy, vacancy defects are expected to be abundant in phosphorene [25]. The variation of formation energy in negatively charged state with the Fermi energy is shown in Fig. 4(g) within DFT (blue dashed line) and DFT+*GW* (blue solid line). The CTL $\varepsilon(0/-1)$ is 0.62 eV above the VBM within DFT and 1.06 eV above the VBM within DFT+*GW*. This implies that vacancy in monolayer phosphorene behaves as a deep acceptor.

IV. DEFECTS IN BILAYER PHOSPHORENE

A. Interstitial

Interstitial in bilayer has a similar structure to that of interstitial in monolayer phosphorene [Figs. 5(a) and 5(b)]. The interstitial atom prefers to bond with two atoms in the outer sublayer of bilayer phosphorene facing vacuum. The configuration with the interstitial atom between the layers is higher in energy by 580 meV per defect. Like the monolayer, spin-polarized calculation on interstitial in bilayer shows that it also induces two defect states in the gap. One of the defect states is filled rendering interstitial to be possible in $+1$, 0, -1 charge states. DOS calculations on the three charge states reveal that while the defect states are nondegenerate in neutral state they become degenerate by accepting or donating an electron in charged states [Fig. 5(c)]. In the neutral charge state, the formation energy is 1.45 eV which is lower than the corresponding defect in the monolayer. The electrostatic

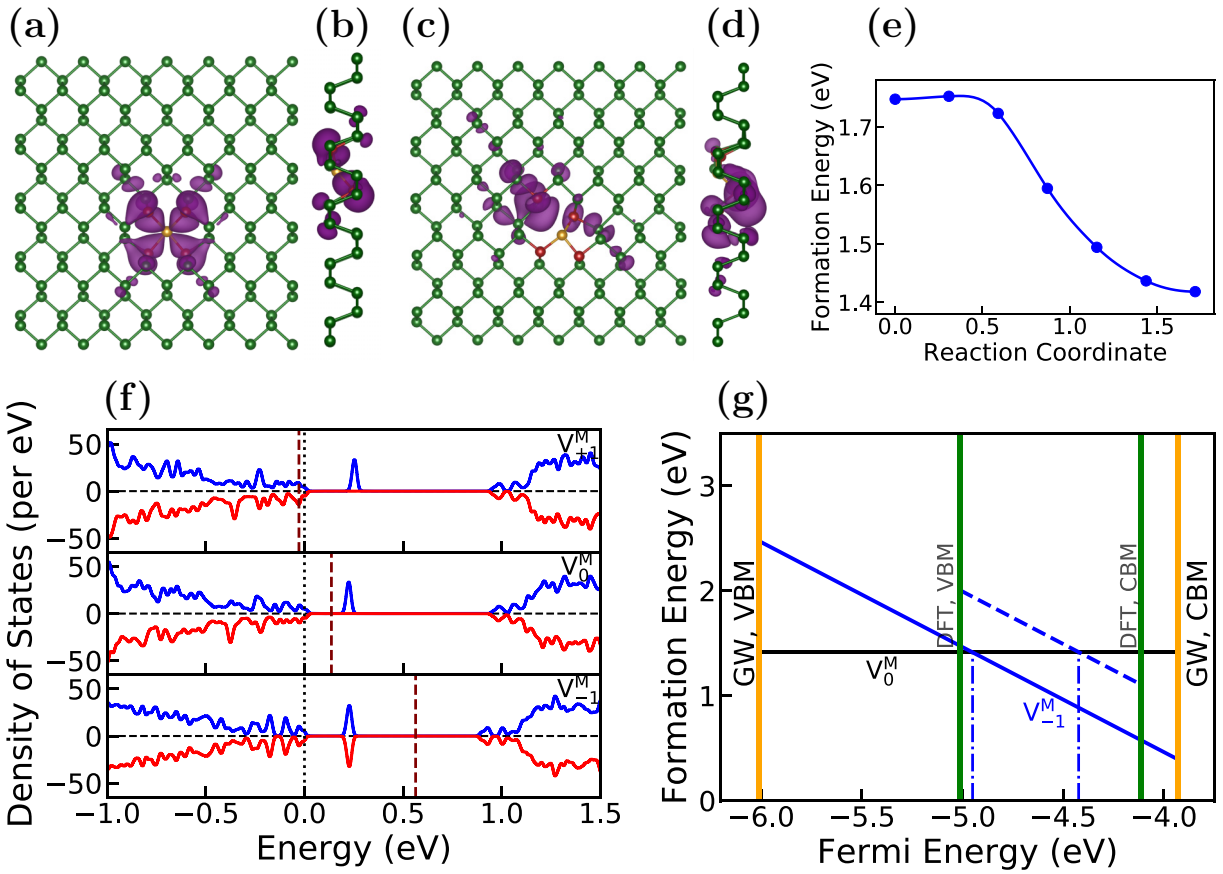

FIG. 4. (a) and (b) show the top and side view of MV-(55|66) in 7×5 supercell and the defect wave function. (c) and (d) show MV-(5|9) and the wave function localized at defect from the top and side view, respectively. The isosurface of wave functions is plotted at 3.4×10^{-3} e/Å^3. The neighbor to the vacancy is shown in yellow and the other neighbor atoms are shown in red. (e) shows the variation of formation energy while the structure changes from MV-(55|66) to MV-(5|9). The reaction coordinate is the distance between two images in hyper-surface. (f) Spin-polarized DOS of vacancy in all three charge states. The red and blue lines denote two spin states. The VBM of the corresponding cells are set to zero and shown in black dotted lines. The maroon dashed lines are Fermi levels of the corresponding systems. (g) depicts the variation of formation energies with Fermi energy both within DFT and DFT+*GW*. The black line is for vacancy in neutral state and negatively charged vacancy is represented by the blue solid (DFT+*GW*) and dashed (DFT) lines.

correction with the model charge is calculated to be 0.167 eV. We include this correction and the potential alignment term to calculate the formation energies in charged states. Figure 5(d) shows the formation energies of interstitial in its three charge states $+1$, 0, and -1 within both DFT and DFT+*GW*. We find the $+1$ charged interstitial is always higher in energy when the Fermi energy is in the band gap in DFT. In contrast, the interstitial is more stable in the positively charged state within DFT+*GW* when the Fermi level is below 0.43 eV with respect to VBM which marks the CTL $\varepsilon(+1/0)$. The CTL $\varepsilon(0/-1)$ is at 0.86 eV (0.33 eV) above VBM within DFT+*GW* (DFT). This suggests that the interstitial in bilayer can act as both donor- and acceptor-type defect like the interstitial defect in monolayer.

B. Vacancy

In bilayer phosphorene, the vacancy can reside in two inequivalent positions. In one configuration the vacancy faces the second layer while in the other it faces vacuum. We found the vacancy is most stable in MV-(5|9) structure facing vacuum [Figs. 6(a) and 6(b)]. Spin-polarized calculation within GGA-PBE on this structure does not show any distinct defect state in the band gap [Fig. 6(c)]. This calculation suggests hybridization between defect state and states inside the valence band edge. However, after a diagonal *GW* correction, a state emerges in the gap. This poses a problem to the diagonal *GW* approximation [Eq. (4)], in which the self-energy matrix element is computed using the DFT wave functions as:

$$E_i^{\mathrm{QP}} = E_i^{\mathrm{DFT}} + \left\langle \psi_i^{\mathrm{DFT}} \middle| \Sigma_{GW}(\{E^{\mathrm{DFT}}, \psi^{\mathrm{DFT}}\}; E^{\mathrm{QP}}) \middle| \psi_i^{\mathrm{DFT}} \right\rangle - \left\langle \psi_i^{\mathrm{DFT}} \middle| \mathrm{V_{XC}} \middle| \psi_i^{\mathrm{DFT}} \right\rangle. \quad (4)$$

One way to overcome this problem is to perform self-consistent *GW* calculation. Another way is to choose a better mean-field. To address the issue we start with an alternative mean-field. We use hybrid functional approximation (HSE) [29] for exchange-correlation which is an improvement over GGA. We relax the vacancy structure with HSE. For all further calculations, the total energies are calculated with HSE. The obtained band structure gives a distinct state in the band gap, however the state is very close to valence bands [Fig. 6(d)]. Vacancy has a formation energy of 0.97 eV in the neutral

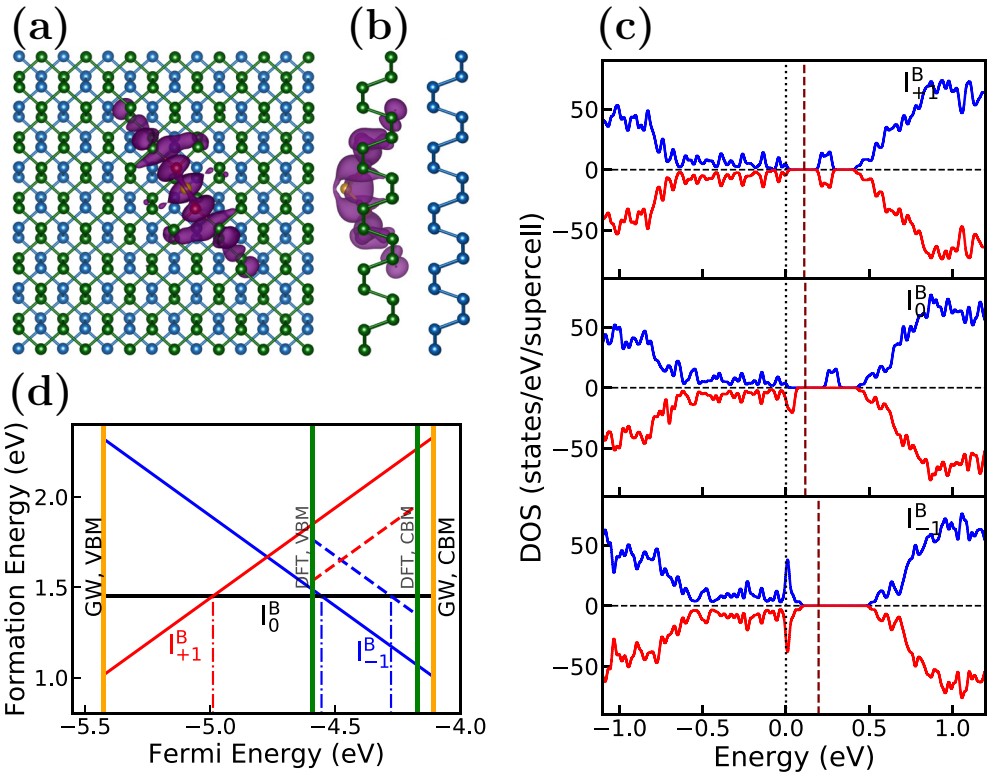

FIG. 5. (a) and (b) are the top and side view of interstitial defect with the localized wave function in bilayer phosphorene. (c) Spin-polarized DOS of interstitial in bilayer phosphorene in positive, neutral, and negative charged states. VBM are set to zero and the Fermi level are shown in maroon dashed line. Red and blue lines represent two spin states. (d) CTLs calculated within both DFT and DFT+*GW*. Solid lines denote the formation energies within DFT+*GW* and the dashed lines are used for DFT. Red, black, and blue are for +1, 0, and −1 charge states. Vacuum is set to zero.

state. The calculated CTL $\varepsilon(0/-1)$ within HSE is at 0.34 eV above VBM [Fig. 6(e)]. For *GW* calculation we choose a configuration such that the defect state is in the gap within HSE. As generating 4300 bands with HSE is computationally expensive and the quasiparticle energies depend weakly on the mean-field used, we generate the wave functions within PBE. The starting PBE defect wave function is localized at the defect site. While the defect state is also in the gap using PBE, because of its proximity to the VBM edge it is expected that the diagonal G_0W_0 approximation is not going to be adequate. We construct the *GW* Hamiltonian in the DFT wave function basis following Eq. (5).

$$H_{ij} = E_i^{\mathrm{DFT}}\delta_{ij} + \left\langle \psi_i^{\mathrm{DFT}} \middle| \Sigma_{GW}(\{E^{\mathrm{DFT}}, \psi^{\mathrm{DFT}}\}; E^{\mathrm{QP}}) \middle| \psi_j^{\mathrm{DFT}} \right\rangle - \left\langle \psi_i^{\mathrm{DFT}} \middle| \mathrm{V_{XC}} \middle| \psi_j^{\mathrm{DFT}} \right\rangle \quad (5)$$

Due to computational cost, we restrict the construction of Hamiltonian matrix with wave functions with energy within ±500 meV of the defect state as we are interested in the defect state and the states close to it. The self-energy matrix is evaluated within static-screening limit (static-COHSEX) [34] and we diagonalize the constructed Hamiltonian [66]. The eigenfunctions of the Hamiltonian are the new wave functions with which we performed G_1W_0 calculation. It should be noted that in this way, the wave functions are iterated while the dielectric screening is still constructed from mean-field wave functions. The quasiparticle energies are obtained by evaluating the self-energy using the standard plasmon pole model. For the vacancy in bilayer, G_0W_0 calculation shows that there is mixing between the defect state and the valence bands close to it. After the first iteration with the updated wave functions, the quasiparticle energy of the defect state is 370 meV away from the VBM edge.

Instead of calculating the CTL using the quasiparticle energy at the equilibrium structure, we can calculate that at any structure and adjust the relaxation energy accordingly (Fig. 7) [67]. We can denote an intermediate structure by $\vec{\mathrm{R}}_{\mathrm{I}}$ and rewrite Eq. (2) in the following way:

$$\varepsilon(q/q') = \frac{\left(E_q^f[\vec{\mathrm{R}}_q] - E_q^f[\vec{\mathrm{R}}_{\mathrm{I}}]\right) + \left(E_q^f[\vec{\mathrm{R}}_{\mathrm{I}}] - E_{q'}^f[\vec{\mathrm{R}}_{\mathrm{I}}]\right) + \left(E_{q'}^f[\vec{\mathrm{R}}_{\mathrm{I}}] - E_{q'}^f[\vec{\mathrm{R}}_{q'}]\right)}{q' - q} \quad (6)$$

$$= E_{\mathrm{relax},q} + E_{\mathrm{QP}} + E_{\mathrm{relax},q'}. \quad (7)$$

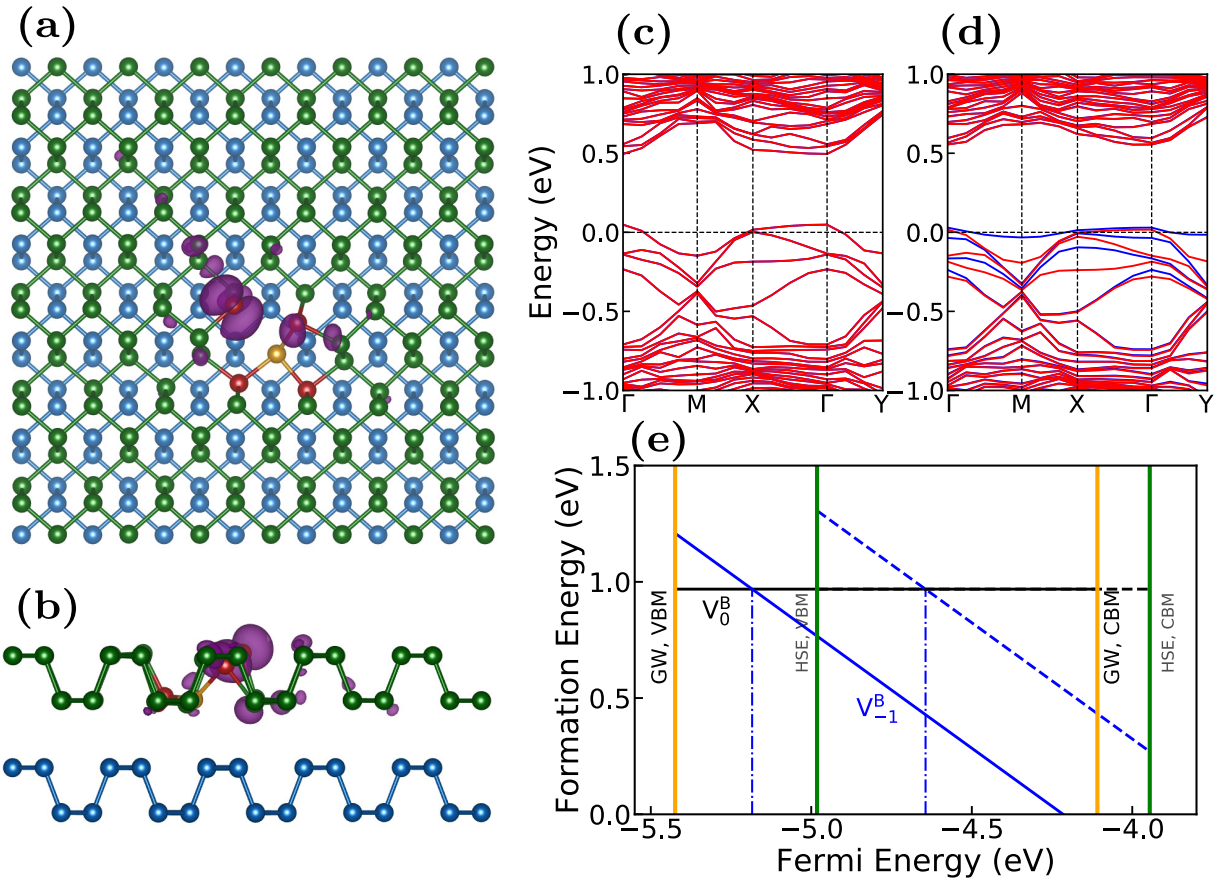

FIG. 6. (a) and (b) show the top and side view of MV-(5|9) in bilayer phosphorene. The defect wave function is plotted at isosurface value of 3.4×10^{-3} e/Å^3. (c) and (d) show the band diagrams of the defect structure relaxed with PBE and HSE, respectively. Red and blue lines denote two spin states. (e) is the formation energy plot of vacancy in neutral and negative state.

Figure 7 shows two energy curves for two charge states of the defect. $\vec{R}_I$ is an intermediate structure at which the quasiparticle energy is calculated (brown straight arrow in Fig. 7). To obtain the CTL, the relaxation energies from the $\vec{R}_I$ to $\vec{R}_q$ and $\vec{R}_{q'}$ (blue curved arrows in Fig. 7) are taken into account. For the vacancy calculation in bilayer phosphorene, we adopt this scheme to calculate the CTL within DFT+*GW*. The intermediate structure is chosen as discussed above. We perform the *GW* calculation with the intermediate structure to get the quasiparticle energy (E_{QP}) and calculate the relaxation energy from that structure to equilibrium neutral and negatively charged structure as the vacancy is stable in neutral and negative state. Using this formalism [Eq. (6)], the CTL $\varepsilon(0/-1)$ is found to be at 0.24 eV with respect to VBM within DFT+*GW* [Fig. 6(e)] which again implies that vacancy in bilayer phosphorene behaves like an acceptor.

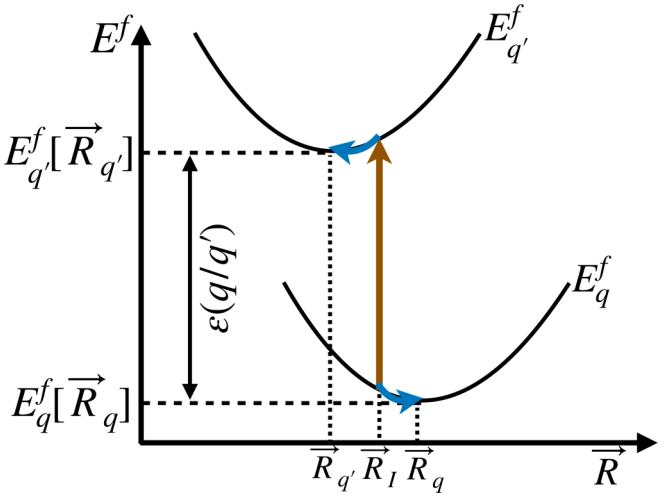

FIG. 7. The figure shows calculation of CTL starting from an intermediate structure. The brown arrow represents the quasiparticle energy calculated at $\vec{R}_I$ and the curved blue arrows are the relaxation energy.

V. CONCLUSION

We have extensively studied the formation and electronic properties of vacancy and self-interstitial defects in mono and bilayer phosphorene. We have taken into account the spurious electrostatic correction while studying charged defects. The defects have formation energies between 0.9–1.6 eV in neutral state. Depending on the charge state, these defects can further lower their formation energies. It has been also observed that the formation energy of defects in bilayer phosphorene is smaller than that in monolayer suggesting that with the

increase of layer number formation energy decreases. We calculate the CTLs of the defects within DFT and DFT+*GW* formalism which suggest that while vacancy behaves as acceptor type defect, interstitial can act as both acceptor and donor type defect.

ACKNOWLEDGMENT

We thank the Supercomputer Education and Research Centre (SERC) at IISc for providing the computational resources.

[1] K. S. Novoselov, A. K. Geim, S. V. Morozov, D. Jiang, Y. Zhang, S. V. Dubonos, I. V. Grigorieva, and A. A. Firsov, Science **306**, 666 (2004).
[2] A. K. Geim and K. S. Novoselov, Nat. Mater. **6**, 183 (2007).
[3] F. V. Kusmartsev, W. M. Wu, M. P. Pierpoint, and K. C. Yung, in *Applied Spectroscopy and the Science of Nanomaterials*, edited by P. Misra (Springer, Singapore, 2015), pp. 191–221.
[4] F. Schedin, A. K. Geim, S. V. Morozov, E. W. Hill, P. Blake, M. I. Katsnelson, and K. S. Novoselov, Nat. Mater. **6**, 652 (2007).
[5] F. Schwierz, Nat. Nanotechnol. **5**, 487 (2010).
[6] K. F. Mak, C. Lee, J. Hone, J. Shan, and T. F. Heinz, Phys. Rev. Lett. **105**, 136805 (2010).
[7] R. Branimir and A. Kis, Nat. Mater. **12**, 815 (2013).
[8] Q. H. Wang, K. Kalantar-Zadeh, A. Kis, J. N. Coleman, and M. S. Strano, Nat. Nanotechnol. **7**, 699 (2012).
[9] B. Radisavljevic, A. Radenovic, J. Brivio, V. Giacometti, and A. Kis, Nat. Nanotechnol. **6**, 147 (2011).
[10] L. Li, Y. Yu, G. J. Ye, Q. Ge, X. Ou, H. Wu, D. Feng, X. H. Chen, and Y. Zhang, Nat. Nanotechnol. **9**, 374 (2014).
[11] H. Liu, A. T. Neal, Z. Zhu, Z. Luo, X. Xu, D. Tománek, and P. D. Ye, ACS Nano **8**, 4033 (2014).
[12] A. Castellanos-Gomez, L. Vicarelli, E. Prada, J. O. Island, K. L. Narasimha-Acharya, S. I. Blanter, D. J. Groenendijk, M. Buscema, G. A. Steele, J. V. Alvarez, H. W. Zandbergen, J. J. Palacios, and H. S. J. van der Zant, 2D Mater. **1**, 025001 (2014).
[13] M. Buscema, D. J. Groenendijk, G. A. Steele, H. S. van der Zant, and A. Castellanos-Gomez, Nat. Commun. **5**, 4651 (2014).
[14] A. Brown and S. Rundqvist, Acta Cryst. **19**, 684 (1965).
[15] F. Xia, H. Wang, and Y. Jia, Nat. Commun. **5**, 4458 (2014).
[16] Z. Luo, J. Maassen, Y. Deng, Y. Du, R. P. Garrelts, M. S. Lundstrom, P. D. Ye, and X. Xu, Nat. Commun. **6**, 8572 (2015).
[17] R. Schuster, J. Trinckauf, C. Habenicht, M. Knupfer, and B. Büchner, Phys. Rev. Lett. **115**, 026404 (2015).
[18] L. Liang, J. Wang, W. Lin, B. G. Sumpter, V. Meunier, and M. Pan, Nano Lett. **14**, 6400 (2014).
[19] M. H. Naik and M. Jain, Phys. Rev. B **95**, 165125 (2017).
[20] J. Qiao, X. Kong, Z.-X. Hu, F. Yang, and W. Ji, Nat. Commun. **5**, 4475 (2014).
[21] S. Das, W. Zhang, M. Demarteau, A. Hoffmann, M. Dubey, and A. Roelofs, Nano Lett. **14**, 5733 (2014).
[22] W. Hu and J. Yang, J. Phys. Chem. C **119**, 20474 (2015).
[23] F. Banhart, J. Kotakoski, and A. V. Krasheninnikov, ACS Nano **5**, 26 (2011).
[24] Y. Liu, F. Xu, Z. Zhang, E. S. Penev, and B. I. Yakobson, Nano Lett. **14**, 6782 (2014).
[25] B. Kiraly, N. Hauptmann, A. N. Rudenko, M. I. Katsnelson, and A. A. Khajetoorians, Nano Lett. **17**, 3607 (2017).
[26] A. A. Kistanov, Y. Cai, K. Zhou, S. V. Dmitriev, and Y.-W. Zhang, 2D Mater. **4**, 015010 (2017).
[27] K. L. Utt, P. Rivero, M. Mehboudi, E. O. Harriss, M. F. Borunda, A. A. Pacheco SanJuan, and S. Barraza-Lopez, ACS Cent. Sci. **1**, 320 (2015).
[28] J. Pei, X. Gai, J. Yang, X. Wang, Z. Yu, D.-Y. Choi, B. Luther-Davies, and Y. Lu, Nat. Commun. **7**, 10450 (2016).
[29] J. Heyd, G. E. Scuseria, and M. Ernzerhof, J. Chem. Phys. **118**, 8207 (2003).
[30] J. P. Perdew, K. Burke, and M. Ernzerhof, Phys. Rev. Lett. **77**, 3865 (1996).
[31] M. Jain, J. R. Chelikowsky, and S. G. Louie, Phys. Rev. Lett. **107**, 216806 (2011).
[32] P. Deák, E. Khorasani, M. Lorke, M. Farzalipour-Tabriz, B. Aradi, and T. Frauenheim, Phys. Rev. B **100**, 235304 (2019).
[33] L. Hedin, J. Phys.: Condens. Matter **11**, R489 (1999).
[34] M. S. Hybertsen and S. G. Louie, Phys. Rev. B **34**, 5390 (1986).
[35] M. Jain, J. R. Chelikowsky, and S. G. Louie, Phys. Rev. Lett. **107**, 216803 (2011).
[36] M. H. Naik and M. Jain, Phys. Rev. Mater. **2**, 084002 (2018).
[37] V. Wang, Y. Kawazoe, and W. T. Geng, Phys. Rev. B **91**, 045433 (2015).
[38] Y. Guo and J. Robertson, Sci. Rep. **5**, 14165 (2015).
[39] D. Wang, D. Han, X.-B. Li, N.-K. Chen, D. West, V. Meunier, S. Zhang, and H.-B. Sun, Phys. Rev. B **96**, 155424 (2017).
[40] J.-H. Yang and B. I. Yakobson, arXiv:1711.05094.
[41] P. Giannozzi, S. Baroni, N. Bonini, M. Calandra, R. Car, C. Cavazzoni, D. Ceresoli, G. L. Chiarotti, M. Cococcioni, I. Dabo, A. D. Corso, S. Gironcoli, S. Fabris, G. Fratesi, R. Gebauer, U. Gerstmann, C. Gougoussis, A. Kokalj, M. Lazzeri, L. Martin-Samos, N. Marzari, F. Mauri, R. Mazzarello, S. Paolini, A. Pasquarello, L. Paulatto, C. Sbraccia, S. Scandolo, G. Sclauzero, A. P. Seitsonen, A. Smogunov, P. Umari, and R. M. Wentzcovitch, J. Phys.: Condens. Matter **21**, 395502 (2009).
[42] D. R. Hamann, M. Schlüter, and C. Chiang, Phys. Rev. Lett. **43**, 1494 (1979).
[43] S. Grimme, J. Comput. Chem. **27**, 1787 (2006).
[44] H. J. Monkhorst and J. D. Pack, Phys. Rev. B **13**, 5188 (1976).
[45] J. Deslippe, G. Samsonidze, D. A. Strubbe, M. Jain, M. L. Cohen, and S. G. Louie, Comput. Phys. Commun. **183**, 1269 (2012).
[46] S. Ismail-Beigi, Phys. Rev. B **73**, 233103 (2006).
[47] J. Deslippe, G. Samsonidze, M. Jain, M. L. Cohen, and S. G. Louie, Phys. Rev. B **87**, 165124 (2013).
[48] See Supplemental Material at http://link.aps.org/supplemental/10.1103/PhysRevMaterials.4.054004 for more details on convergence parameters for *GW* calculation and calculation of electrostatic correction to formation energy.
[49] F. Ferreira and R. M. Ribeiro, Phys. Rev. B **96**, 115431 (2017).

[50] V. Tran, R. Soklaski, Y. Liang, and L. Yang, Phys. Rev. B **89**, 235319 (2014).
[51] V. Tran, R. Fei, and L. Yang, 2D Mater. **2**, 044014 (2015).
[52] X. Wang, A. M. Jones, K. L. Seyler, V. Tran, Y. Jia, H. Zhao, H. Wang, L. Yang, X. Xu, and F. Xia, Nat. Nanotechnol. **10**, 517 (2015).
[53] A. Stathopoulos and J. R. McCombs, ACM Trans. Math. Softw. **37**, 21:1 (2010).
[54] L. Wu, E. Romero, and A. Stathopoulos, SIAM J. Sci. Comput. **39**, S248 (2017).
[55] C. Freysoldt, J. Neugebauer, and C. G. Van de Walle, Phys. Rev. Lett. **102**, 016402 (2009).
[56] M. H. Naik and M. Jain, Comput. Phys. Commun. **226**, 114 (2018).
[57] J.-Y. Noh, H. Kim, and Y.-S. Kim, Phys. Rev. B **89**, 205417 (2014).
[58] E. J. G. Santos and E. Kaxiras, Nano Lett. **13**, 898 (2013).
[59] H.-P. Komsa, N. Berseneva, A. V. Krasheninnikov, and R. M. Nieminen, Phys. Rev. X **4**, 031044 (2014).
[60] H.-P. Komsa, N. Berseneva, A. V. Krasheninnikov, and R. M. Nieminen, Phys. Rev. X **8**, 039902(E) (2018).
[61] C. A. Rozzi, D. Varsano, A. Marini, E. K. U. Gross, and A. Rubio, Phys. Rev. B **73**, 205119 (2006).
[62] A. Malashevich, M. Jain, and S. G. Louie, Phys. Rev. B **89**, 075205 (2014).
[63] W. Chen and A. Pasquarello, J. Phys.: Condens. Matter **27**, 133202 (2015).
[64] F. Wu, A. Galatas, R. Sundararaman, D. Rocca, and Y. Ping, Phys. Rev. Mater. **1**, 071001 (2017).
[65] S. Kundu, S. Bhattacharjee, S.-C. Lee, and M. Jain, Comput. Phys. Commun. **233**, 261 (2018).
[66] M. Jain, J. Deslippe, G. Samsonidze, M. L. Cohen, J. R. Chelikowsky, and S. G. Louie, Phys. Rev. B **90**, 115148 (2014).
[67] T. Biswas and M. Jain, Phys. Rev. B **99**, 144102 (2019).